RSC Advances

PAPER

View Article Online
View Journal | View Issue

Cite this: *RSC Adv.*, 2026, **16**, 12948

Using PdO-incorporated MOF-derived sandwich heterostructures for enhanced glucose sensing

Jiaxi Li,[a] Chen Chen,*[b] Zirong Tang,[c] Guanglan Liao,*[ac] Lei Nie[a] and Tielin Shi[c]

Blood glucose concentration plays a vital role in the clinical diagnosis and therapeutic monitoring of diabetes mellitus. Accurate measurement and continuous monitoring of glucose levels are essential for effective disease prevention and management. However, conventional detection methods face significant limitations in practical applications due to poor stability and sensitivity, which hinders the development of long-term continuous glucose monitoring. Herein, we demonstrate novel PdO-incorporated MOF-derived sandwich heterostructures, Co_3O_{4-10}@PdO_5@CoCu oxides$_{-400}$, for glucose sensing. The incorporation of PdO facilitates electron transfer, thereby significantly enhancing the sensitivity of glucose detection. Notably, the unique sandwich structure effectively prevents the leaching of PdO during electrochemical cycling and improves detection stability, enabling the electrode to retain 93.73% of the initial current response after 30 days. The MOF-derived heterostructure, induced by structural transformation in the annealing process, exposes additional active sites and further enhances the electrochemical activity. The experimental results exhibit exceptional sensing performance, with high sensitivities (4.372 mA mM^{-1} cm^{-2} and 2.615 mA mM^{-1} cm^{-2}). The linear ranges (0.01–1 mM; 1–2.5 mM) and low detection limit (1.49 μM) effectively cover the trace glucose levels typical of human sweat, fulfilling the sensitivity requirements for non-invasive monitoring. Additionally, the rapid response time (2.35 s) ensures immediate signal readout, satisfying the efficiency demands for practical applications. Our work presents a promising approach for developing highly stable and sensitive electrode structures, laying the foundation for future continuous glucose monitoring applications.

Received 25th December 2025
Accepted 28th February 2026

DOI: 10.1039/d5ra10005d

rsc.li/rsc-advances

Open Access Article. Published on 09 March 2026. Downloaded on 4/7/2026 1:56:55 PM.
This article is licensed under a Creative Commons Attribution-NonCommercial 3.0 Unported Licence.

Introduction

Diabetes, recognized by the World Health Organization as one of the four major non-communicable diseases, is associated with severe complications, including nephropathy, retinopathy, and cardiovascular diseases.[1] According to projections, the global population affected by diabetes is expected to reach 700 million by 2045.[2] The concentration of glucose is a critical indicator for assessing glucose metabolism in the human body, which is essential for screening and monitoring conditions such as diabetes and hypoglycaemia. Consequently, the development of advanced electrode structures with high stability and fast response time is the critical prerequisite for continuous and real-time glucose monitoring. Electrochemical sensing has emerged as a promising approach for glucose detection due to its high sensitivity, excellent selectivity, ease of integration, and potential for continuous monitoring.[3–6] The performance of electrochemical glucose sensing heavily depends on the choice of electrode materials. While enzyme-based materials have been widely utilized for glucose detection owing to their high selectivity, recent advancements have shifted focus toward non-enzymatic electrode materials.[7–10] This phenomenon is primarily attributed to the fact that non-enzymatic sensing technologies provide high stability, which could resist environmental interference for long-time continuous monitoring.[11–13]

Metal–organic frameworks (MOFs), which are porous crystalline materials formed through the self-assembly of metal nodes and organic ligands, are considered a new material option for non-enzymatic sensing due to their unique pore structure, high specific surface area, and abundant active sites.[4,14,15] In particular, ZIF-L, a two-dimensional MOF with a leaf-like morphology, offers abundant exposed edge sites and high surface accessibility, making it easier to modify and suitable for constructing sensing structures.[16] However, their practical application has been hindered by inherent limitations, such as insufficient electrical conductivity and the presence of inaccessible active sites. To further enhance their performance in practical applications, MOF derivatives, particularly metal

---

[a] *Hubei Modern Manufacturing Quality Laboratory, School of Mechanical Engineering, Hubei University of Technology, Wuhan 430068, China. E-mail: guanglan.liao@hust.edu.cn*

[b] *Naval University of Engineering, Wuhan, 430033, China. E-mail: 2420242078@nue.edu.cn*

[c] *School of Mechanical Science & Engineering, Huazhong University of Science and Technology, Wuhan 430074, China*

© 2026 The Author(s). Published by the Royal Society of Chemistry

Open Access Article. Published on 09 March 2026. Downloaded on 4/7/2026 1:56:55 PM. This article is licensed under a Creative Commons Attribution-NonCommercial 3.0 Unported Licence.

oxides, have been explored through thermal treatment or chemical conversion.[17,18] These derived materials retain the advantageous porous characteristics of MOFs while achieving improved conductivity and catalytic activity. As a result, MOF-derived materials demonstrate considerable potential for advancing the field of non-enzymatic electrochemical sensing.[19,20]

The synergistic or electronic effects between different metal ions have been utilized by combining noble metals and transition metals, to improve the overall performance of non-enzymatic electrochemical sensing.[21–23] In 2023, Huang *et al.*[24] reported a novel MOF structure on gold wires modified with single-walled carbon nanotubes, which exhibited a low detection limit (LOD) of 0.16 μM within a linear range of 0.001–3 mM. Concurrently, Han *et al.*[25] constructed three non-enzymatic electrochemical glucose sensors with bimetallic structures. Among these, the Cu-MOF/PtNPs on gold electrodes displayed excellent glucose catalytic performance, with a sensitivity of 158.41 μA mM^{-1} cm^{-2} and LOD of 0.06 mM, attributed to synergistic amplification within the linear range of 0.40–25.00 mM. However, the inherent high surface energy of noble metals leads to their thermodynamic instability and susceptibility to aggregation, which results in the loss of catalytic activity. To address these issues, a method involving the encapsulation of noble metal nanoparticles with catalytically active MOFs has emerged. This heterogeneous structure is referred to as a "sandwich-type" structure.[26] Stabilization of precious metal nanoparticles is achieved by the multiple coordination sites of MOFs and a well-defined pore structure that provides spatial confinement and prevents aggregation.[4,27] In 2022, Zhang *et al.*[26] utilized the sandwich-type UiO-66-NH$_2$@-Pt@PCN-222 nanocomposite as a synergistic catalytic system to selectively reduce nitro benzaldehyde to nitro benzyl alcohol. The PCN-222 shell layer not only provided active sites but also protected the metal nanoparticles, maintaining the activity of catalyst during cycling. Compared to single-component nanostructures, sandwich-type core–shell nanostructures typically exhibit better chemical and physical properties. These structures benefit from synergistic interactions between the inner and outer layers, leading to enhanced functionalities and improved glucose sensing performance.[22] However, few studies focused on designing structures that simultaneously exploit metal synergy, structural reinforcement, and structural transformation to achieve high-performance glucose sensing.

In this study, sandwich structured Co_3O_{4-10}@PdO_5@CoCu oxides$_{\text{-}400}$ derived from MOF were constructed by doping with PdO. The effect of the molar concentration of PdO on the sensitivity of glucose sensing was investigated. Furthermore, a sandwich-type structure was incorporated, and the influence of the outer layer thickness on the doping stability was evaluated. Additionally, the impact of the structural transformation induced by annealing temperature on the electrochemical activity of MOF derivatives was systematically studied. Our electrode demonstrated excellent stability, high sensitivity, and a rapid response time within the physiological glucose concentration range relevant to human sweat. These findings established a highly stable glucose sensing structure as a material candidate, providing a critical stability foundation for future non-invasive monitoring systems.

Materials and methods

Materials

Carbon cloth was obtained from WOS 1009 CeTech Co.; sodium hydroxide (NaOH), ethylene glycol (EG), $PdCl_2$, 2-methylimidazole (Hmim), L-ascorbic acid (AA) and D-fructose (Fr) were procured from MacLean. Ammonium persulfate ($NH_4S_2O_8$), cobalt nitrate hexahydrate ($Co(NO_3)_2 \cdot 6H_2O$), and glucose were sourced from Sigma-Aldrich Chemical Company. Dopamine hydrochloride (DA), uric acid (UA), and folic acid (FA) were acquired from Meilun Biological. All chemicals used in this study were of analytical grade. All solutions were prepared with deionized water obtained from a Milli-Q water purification system.

Characterization

The electrochemical tests were performed utilizing the CS310 electrochemical workstation, with an Ag/AgCl (CHI111) electrode employed as the reference electrode. The samples underwent morphological and structural analysis *via* scanning electron microscopy (SEM) and transmission electron microscopy (TEM). Crystallographic characterization was carried out using Cu-Kα radiation X-ray diffraction (XRD) on a PANalytical B.V. instrument. X-ray photoelectron spectroscopy (XPS) analysis was conducted on a VG MultiLab2000 system utilizing a single Al-Kα X-ray source. Thermogravimetric analysis (TGA) was performed utilizing a Netzsch STA 449 thermogravimetric analyzer with a heating rate of 10 °C min^{-1} in air.

Synthesis

Preparation of $Cu(OH)_2$/carbon cloth. The synthesis method of $Cu(OH)_2$/carbon cloth was based on a previous report and can be described as follows.[19] Initially, a piece of carbon cloth was immersed in 6% white vinegar for 2 h. Subsequently, the carbon cloth was cleaned with ethanol and water for 5 min with the assistance of ultrasound and dried at 60 °C. Then, the carbon cloth was placed into the magnetron sputtering system, where a layer of copper was deposited on its surface at a power of 100 W, and the process lasted for 30 min. Upon completion of the copper deposition step, the Cu/carbon cloth was immersed in a mixture containing NaOH (0.375 M, 200 mL) and $(NH_4)_2S_2O_8$ (0.015 M, 200 mL) at a controlled temperature of 30 °C for 1 h, and then $Cu(OH)_2$/carbon cloth was obtained.

Preparation of CuCo-ZIF-L. $Co(NO_3)_2 \cdot 6H_2O$ (0.08 M) was dissolved in 40 mL of water, followed by the immersion of $Cu(OH)_2$/carbon cloth in the above solution for 5 min. Subsequently, 40 mL of Hmim (0.01 M) was immediately added to the aforementioned solution, which was then kept at a constant temperature of 30 °C for a duration of 2 h. Finally, CuCo-ZIF-L was obtained by drying at 60 °C. The sample was put into a tube furnace and calcined at 400 °C for 4 h at a heating rate of 10 °C min^{-1} in air. Then CoCu oxides$_{\text{-}400}$ were prepared.

Open Access Article. Published on 09 March 2026. Downloaded on 4/7/2026 1:56:55 PM. This article is licensed under a Creative Commons Attribution-NonCommercial 3.0 Unported Licence.

Preparation of PdO_x@CuCo-ZIF-L. $PdCl_2$ at concentrations of 0, 2.5, 5, and 10 mM was dissolved in a mixture of water (8 mL) and ethylene glycol (12 mL) with thorough stirring. Subsequently, CuCo-ZIF-L was transferred to the aforementioned solution and kept at room temperature for 15 min. Then, PdO_x@CuCo-ZIF-L was prepared. The samples, named PdO_x@CuCo-ZIF-L ($x = 0$, 2.5, 5, 10), were subjected to calcination at 400 °C for 4 h in air, thereby obtaining PdO_x@CoCu oxides$_{\text{-}400}$.

Preparation of sandwich ZIF-L$_{\text{-}y}$@PdO_5@CuCo-ZIF-L. The synthesis conditions of Co_3O_{4-y}@PdO_5@CoCu oxides$_{\text{-}400}$ were similar to those of PdO_x@CoCu oxides$_{\text{-}400}$. The difference was in the immersion of the prepared PdO_5@CuCo-ZIF-L in a solution of Hmim and $Co(NO_3)_2\cdot 6H_2O$, where it was kept for 5, 10, 20 and 40 min under controlled temperature conditions of 30 °C. These samples were named as ZIF-L$_{\text{-}y}$@PdO_5@CuCo-ZIF-L ($y =$ 5, 10, 20, 40). Finally, the above samples were transferred to a tubular furnace and calcined at 400 °C for 4 h in air to obtain $Co_3O_{4\text{-}y}$@PdO_5@CoCu oxides$_{\text{-}400}$. For comparison, ZIF-L$_{\text{-}10}$-@PdO_5@CuCo-ZIF-L was calcined at 300, 400, and 500 °C to obtain Co_3O_{4-10}@PdO_5@CoCu oxides$_{\text{-}z}$ ($z = 300, 400, 500$).

Results and discussion

The formation process of sandwich heterostructures was illustrated in Scheme 1. Initially, the pretreated carbon cloth was placed into a magnetron sputtering system to deposit a uniform Cu layer on its surface. Dense $Cu(OH)_2$ nanowires were grown on the surface of Cu by a wet chemical method. Two-dimensional leaf-like CuCo-ZIF-L was synthesized through an ion exchange technology, while $Cu(OH)_2$ acted as a precursor. Subsequently, PdO was incorporated onto the surface of CuCo-ZIF-L, and the impact of varying concentrations of PdO on glucose sensing performance was investigated. Building on this, a sandwich-structured ZIF-L$_{\text{-}y}$@PdO_x@CuCo-ZIF-L was produced *via* epitaxial growth, using PdO_x@CuCo-ZIF-L as the core. The influence of the thickness of the sandwich outer layer ZIF-L on sensing stability of the doped system was emphasized. Finally, Co_3O_{4-y}@PdO_x@CoCu oxides$_{\text{-}z}$ nanosheet arrays were obtained through an annealing process, which removed the surface organic structures and exposed more active sites.

The structural evolution from the MOF precursor to Co_3O_{4-10}-@PdO_5@CoCu oxides$_{\text{-}400}$ was characterized using SEM, as shown in Fig. 1. Initially, the MOF precursor CuCo-ZIF-L exhibited a uniform leaf-like structure which was grown *in situ* on the surface of carbon cloth using $Cu(OH)_2$, as depicted in Fig. 1(a). Upon the incorporation of PdO, irregular nanoparticles appeared on the previously smooth surface of CuCo-ZIF-L, surrounded by an etched-like appearance, as illustrated in Fig. 1(b). In the case of ZIF-L$_{\text{-}10}$@PdO_5@CuCo-ZIF-L, the irregular nanoparticles became less visible due to the coating effect of the outer ZIF-L layer, as depicted in Fig. 1(c). After annealing, the derived Co_3O_{4-10}-@PdO_5@CoCu oxides$_{\text{-}400}$ exhibited a distinct layered structure, as presented in Fig. 1(d). The surface of this structure was densely populated with nanoparticles, which facilitated the exposure of numerous active sites. Throughout the synthesis process, the overall dimensions of the CuCo-ZIF-L derivatives remained relatively consistent, with each structure maintaining a leaf-like morphology approximately 1 μm in size. The crystal structure of Co_3O_{4-10}@PdO_5@CoCu oxides$_{\text{-}400}$ was further investigated by TEM, as illustrated in Fig. 1(e). Lattice spacings of 0.252 nm and 0.232 nm corresponded to the (1 1 1) and (1 1 1) planes of CuO (JCPDS 48-1548), respectively. A lattice spacing of 0.201 nm corresponded with the (4 0 0) plane of CoO (JCPDS 43-1003). A lattice spacing of 0.264 nm matched well with the (1 0 1) plane of PdO (JCPDS 41-1107).

To further elucidate the elemental distribution within the doped structure, TEM elemental mapping was conducted, as shown in Fig. S1. The images reveal that Cu, Co, and Pd elements are uniformly distributed across the entire leaf-like nanostructure. Specifically, the homogeneous dispersion of Pd

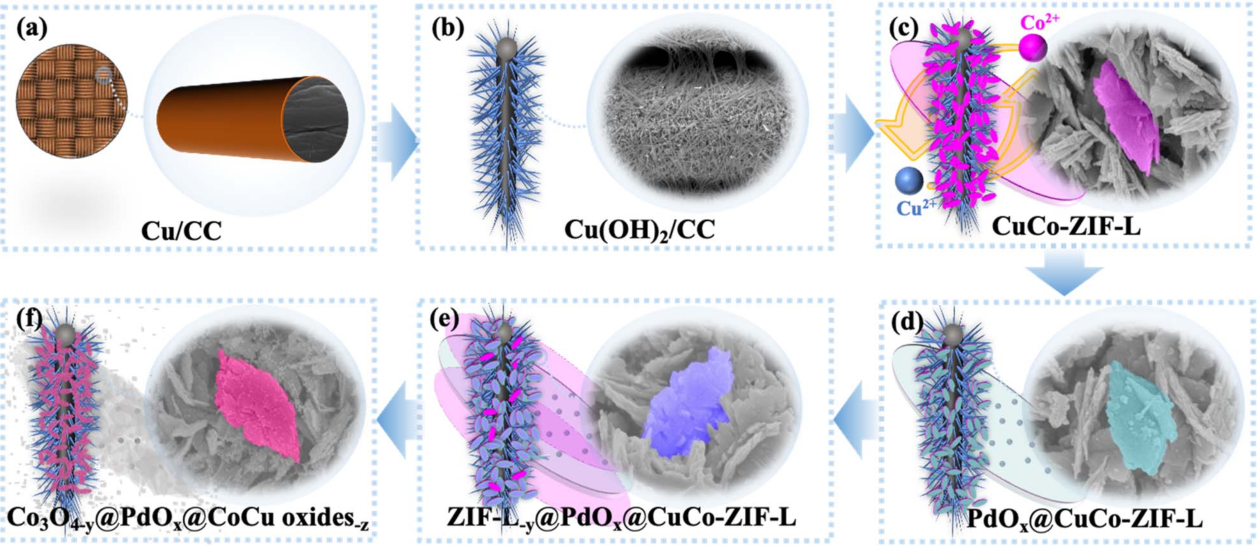

Scheme 1 Schematic illustration of the fabrication process for (a) Cu/CC, (b) $Cu(OH)_2$/CC, (c) CuCo-ZIF-L, (d) PdO_x@CuCo-ZIF-L, (e) ZIF-L$_{\text{-}y}$@-PdO_x@CuCo-ZIF-L, and (f) Co_3O_{4-y}@PdO_x@CoCu oxides$_{\text{-}400}$.

Open Access Article. Published on 09 March 2026. Downloaded on 4/7/2026 1:56:55 PM.
This article is licensed under a Creative Commons Attribution-NonCommercial 3.0 Unported Licence.

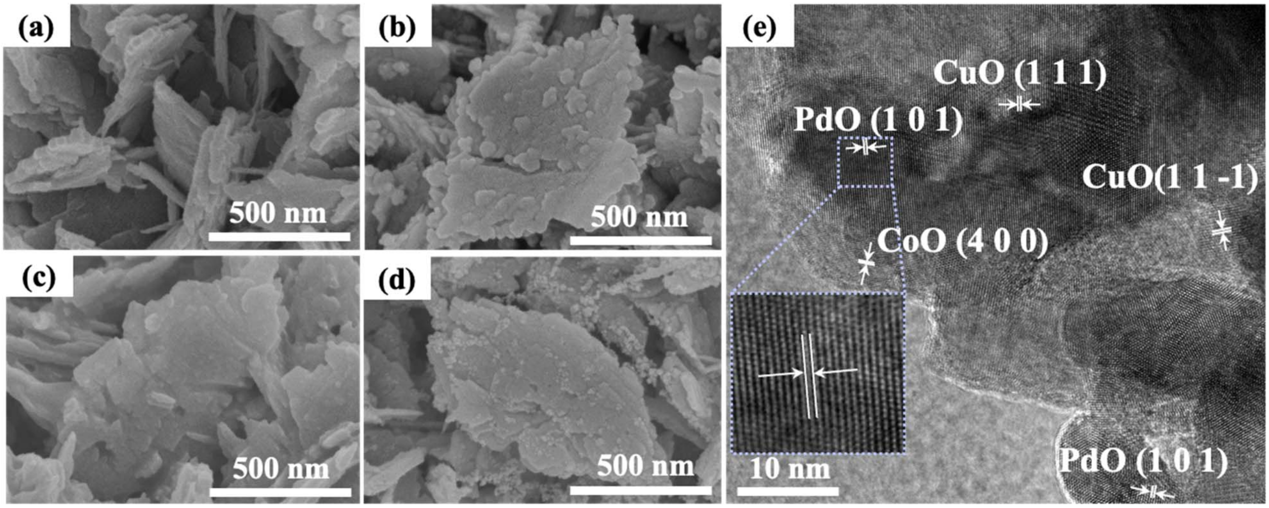

Fig. 1 Morphological characterization of the synthesized materials: SEM images of (a) CuCo-ZIF-L precursor, (b) PdO_5@CuCo-ZIF-L, (c) ZIF-L_{-10}@PdO_5@CuCo-ZIF-L, and (d) Co_3O_{4-10}@PdO_5@CoCu oxides$_{-400}$, and (e) TEM image of Co_3O_{4-10}@PdO_5@CoCu oxides$_{-400}$.

element confirms that the doping process successfully incorporated Pd into the framework without discernible aggregation, validating the effectiveness of the synthesis strategy.

To verify the structural evolution during the synthesis process, XRD results of the intermediates were analyzed, as shown in Fig. S2. The peak located at approximately 25.6° is attributed to the amorphous carbon of the substrate. The diffraction peak at 43.3° corresponds to the metallic Cu layer.[17] For the $Cu(OH)_2$ precursor, characteristic peaks are observed at 16.7°, 23.8°, 34.1°, 38.1°, and 53.5°, which are indexed to the (0 2 0), (0 2 1), (0 0 2), (0 4 1), and (1 5 0) planes of $Cu(OH)_2$, respectively. Upon the formation of the MOF structure, new diffraction peaks emerge at 10.8°, 16.5°, and 17.8°, corresponding to the (3 1 0), (2 0 0), and (2 2 2) crystal planes of CuCo-ZIF-L.[27,28] These results confirm the successful transformation from the precursor to the sandwich-structured MOF composites.

Subsequently, to elucidate the composition of the final glucose sensing structure, XRD analysis was performed on the derived Co_3O_{4-10}@PdO_5@CoCu oxides$_{-400}$, as displayed in Fig. 2(a). A peak around 25.6° corresponded to amorphous carbon. Distinct diffraction peaks at 35.5° and 38.7° matched the (0 0 2) and (1 1 1) crystal planes of CuO, respectively. Additionally, a peak at 36.8° corresponded well with the (3 1 1) crystal plane of Co_3O_4. The characteristic peak at 33.9° aligned perfectly with the (1 0 1) plane of PdO, indicating effective loading of PdO. The XRD pattern manifested that the resulting samples were mainly composed of CuO, Co_3O_4, and PdO, which were in agreement with the results of TEM. The emergence of characteristic diffraction peaks for CuO, Co_3O_4, and PdO, along with the absence of ZIF-L characteristic peaks, confirmed the complete conversion of the MOF precursors into metal oxides.

To further investigate the thermal decomposition behavior of the MOF precursors and determine the optimal annealing temperature, TGA was conducted on CuCo-ZIF-L, PdO_5@CuCo-ZIF-L, and ZIF-L_{-10}@PdO_5@CuCo-ZIF-L, as illustrated in Fig. 2(b). The weight-loss profiles of CuCo-ZIF-L and ZIF-L_{-10}-@PdO_5@CuCo-ZIF-L were similar and could be categorized into two stages. Below 330 °C, a slight weight-loss primarily resulted from the evaporation of H_2O and decomposition of organic molecules on the surface. At temperatures exceeding 450 °C, a significant weight-loss occurred due to the collapse of carbon cloth and other molecules in the structure except for the metals. PdO_5@CuCo-ZIF-L exhibited two weight-loss steps. The first step, occurring below 115 °C, was mainly related to the removal of H_2O and solvent molecules. When the temperature rose above 450 °C, the decomposition of organic components and the skeleton was observed. Notably, PdO_5@CuCo-ZIF-L exhibited a faster weight-loss rate compared to CuCo-ZIF-L, which can be attributed to the catalytic effect of PdO doping, accelerating the decomposition of organic components in CuCo-ZIF-L.[29] In contrast, ZIF-L_{-10}@PdO_5@CuCo-ZIF-L demonstrated a significantly slower weight loss process than PdO_5@CuCo-ZIF-L, implying that the outer ZIF-L shell effectively protected PdO from exfoliation and aggregation while retarding the decomposition of organic components. Based on these findings, the annealing temperature for CuCo-ZIF-L was set at 400 °C to remove surface organics with the ZIF-L skeleton preserved and more active sites exposed. The distinct weight loss stages in TGA curves, corresponding to the decomposition of organic ligands, clearly validated the structural transformation from MOF precursors to metal oxides.[30]

The elemental valence states and surface chemical compositions of the MOF-derived Co_3O_{4-10}@PdO_5@CoCu oxides$_{-400}$ were analyzed by XPS, which confirmed the presence of C, O, Cu, Co, and Pd elements, as depicted in Fig. 2(c). In the spectrum of Cu 2p (Fig. 2(d)), the primary peaks observed at 933.60 eV (Cu $2p_{3/2}$) and 953.70 eV (Cu $2p_{1/2}$), along with satellite peaks at 962.33 eV, 943.93 eV, and 941.52 eV, confirmed the presence of Cu^{2+}. In the spectrum of Co 2p (Fig. 2(e)), two distinct peaks at 780.10 eV and 798.90 eV were identified, corresponding to the Co $2p_{3/2}$ and Co $2p_{1/2}$ peaks of Co_3O_4. The

Open Access Article. Published on 09 March 2026. Downloaded on 4/7/2026 1:56:55 PM.
This article is licensed under a Creative Commons Attribution-NonCommercial 3.0 Unported Licence.

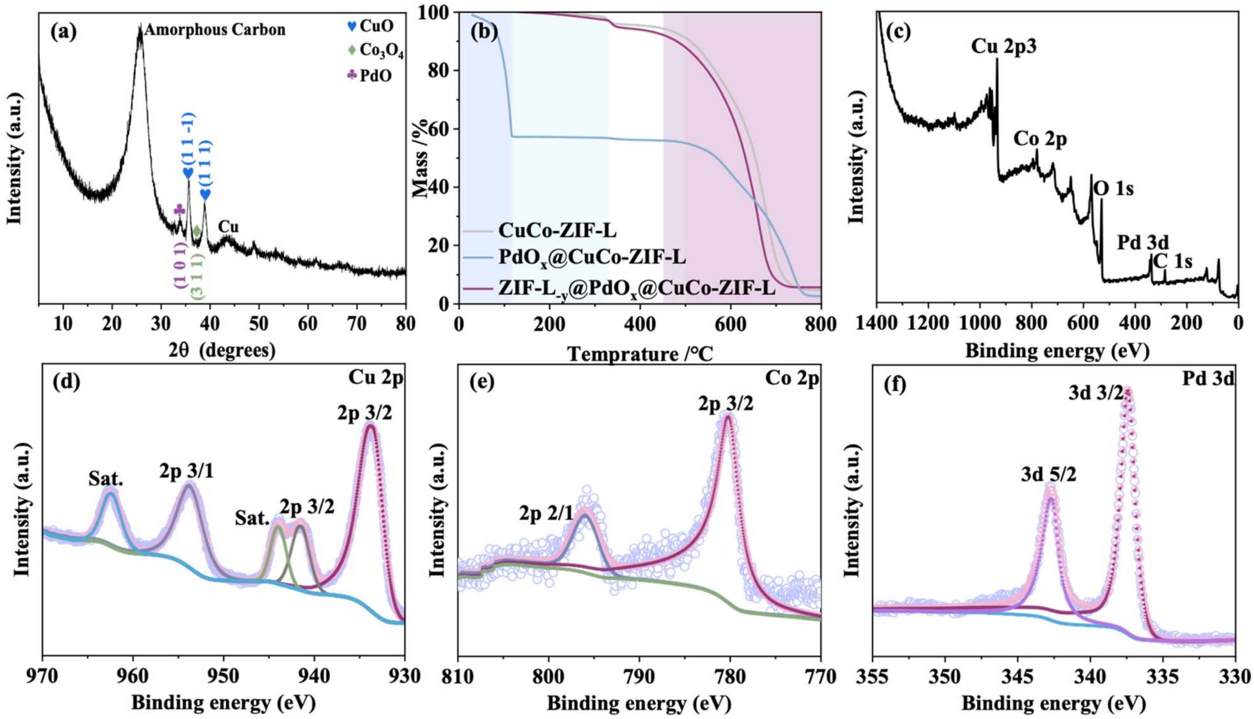

Fig. 2 Structural and compositional characterization of Co$_3$O$_{4-10}$@PdO$_5$@ CoCu oxides$_{-400}$: (a) XRD pattern, (b) TGA curve, high-resolution XPS (c) survey spectra, (d) Cu 2p, (e) Co 2p, (f) Pd 3d.

spectrum of Pd 3d (Fig. 2(f)) displayed two major peaks at 337.50 eV and 342.50 eV, which were assigned to Pd 3d$_{5/2}$ and Pd 3d$_{3/2}$ in PdO, respectively. These findings are consistent with the XRD results, further validating the successful formation of the desired phases.

Additionally, to investigate the influence of PdO doping concentration on the morphological evolution of MOF nanostructures and to precisely control the doping process, the samples with three different doping concentrations of PdO were studied, as displayed in Fig. S3. Firstly, the pristine CuCo-ZIF-L exhibited a characteristic leaf-like morphology with a relatively smooth surface. Upon introducing a PdO doping concentration of 2.5 mM, the resulting PdO$_{2.5}$@CuCo-ZIF-L showed significant surface etching, leading to the formation of nanocrystalline structures. When the doping concentration was increased to 5 mM, the leaf-like architecture underwent further etching, accompanied by the emergence of numerous nanoparticles on the surface. Notably, with a PdO doping concentration of 10 mM, the original leaf-like structure of CuCo-ZIF-L was completely disrupted. These observations revealed that the doping concentration of PdO played a crucial role in modulating the morphology of MOFs. The observed morphological changes can be attributed to the synergistic interactions between the metal constituents, where the controlled variation in PdO doping concentration induces progressive etching of CuCo-ZIF-L, consequently increasing the specific surface area and exposing additional active sites.

Further, the impact of the thickness of the sandwich outer layer on the morphology of ZIF-L$_{-y}$@PdO$_5$@CuCo-ZIF-L was explored, as shown in Fig. S4. The morphological analysis revealed a distinct correlation between the shell layer coating duration and the resulting nanostructure dimensions. Specifically, ZIF-L$_{-5}$@PdO$_5$@CuCo-ZIF-L, synthesized with a 5 min coating duration, maintained the characteristic leaf-like morphology with a measured thickness of approximately 90 nm, representing a 10 nm increase compared to the uncoated PdO$_5$@CuCo-ZIF-L. Upon extending the coating duration to 10 min, ZIF-L$_{-10}$@PdO$_5$@CuCo-ZIF-L exhibited a more pronounced leaf-like structure with a thickness of approximately 125 nm. Further prolongation of the coating time to 20 min resulted in ZIF-L$_{-20}$@PdO$_5$@CuCo-ZIF-L displaying enhanced hierarchical architecture with a substantial thickness increase to approximately 200 nm. Notably, when the time was further extended to 40 min, the thickness grew to approximately 300 nm, while the loaded PdO was completely encapsulated. These observations suggest that the thickness of the outer layer of the MOF significantly affects the morphology and size of the prepared sensing structures. The well-defined pore structure of the sandwich MOF provided diffusion channels, accelerating the transfer of glucose molecules and intermediates.

The thermal induced structural transformation of the CuCo-ZIF-L, PdO$_5$@CuCo-ZIF-L, and ZIF-L$_{-10}$@PdO$_5$@CuCo-ZIF-L was studied through SEM. The structures of the samples were transformed with the basic morphology and dimensions retained, as depicted in Fig. S5. The thermally treated CoCu oxides$_{-400}$ exhibited a porous architecture with numerous well-distributed micropores on the surface. PdO$_5$@CoCu oxides$_{-400}$ were transformed into a leaf-like structure composed of

© 2026 The Author(s). Published by the Royal Society of Chemistry

Open Access Article. Published on 09 March 2026. Downloaded on 4/7/2026 1:56:55 PM.
This article is licensed under a Creative Commons Attribution-NonCommercial 3.0 Unported Licence.

interconnected nanoparticles, a structural modification that can be primarily attributed to the incorporation of PdO. Remarkably, Co_3O_{4-10}@PdO_5@CoCu oxides$_{-400}$ demonstrated a more refined nanostructure, consisting of smaller nanocrystals compared to the PdO_5@CoCu oxides$_{-400}$. This morphological refinement is ascribed to the protective effect of the MOF coating, which effectively inhibited the aggregation of PdO during the sintering process, thereby promoting superior dispersion on the MOF surface. Furthermore, the sandwich MOF architecture underwent a complex structural reorganization during thermal annealing, resulting in the formation of hierarchical nanostructures with enhanced specific surface area and increased accessibility of active sites.

The electrochemical performance of the prepared electrode was systematically evaluated, as shown in Fig. 3. CV tests were conducted on the sensing structure in a 0.1 M NaOH solution. It is observed that the peak anode current increased proportionally with the square root of the scanning rate, which suggested that the diffusion-controlled process was occurring on the Co_3O_{4-10}@PdO_5@CoCu oxides$_{-400}$ during the redox reaction. The operating voltage during the assay was an important factor, which plays a role in the catalytic performance of glucose sensing. In order to obtain the optimal current response, the *i*–*t* test of Co_3O_{4-10}@PdO_5@CoCu oxides$_{-400}$ exhibited a step response at different applied potentials ranging from 0.45–0.6 V, with glucose continuously added into a 0.1 M NaOH solution, displayed in Fig. 3(b). As the potential increased from 0.45 V–0.55 V, the current response gradually increased. However, when the potential was set to 0.6 V, a slight decrease in current was observed. Therefore, 0.55 V was selected as the optimal potential for the non-enzymatic glucose sensing in this work. With the continuous addition of glucose (0.01–2.5 mM), the *i*–*t* response of the Co_3O_{4-10}@PdO_5@CoCu oxides$_{-400}$ exhibited a stepwise and gradual enhancement, as illustrated in Fig. 3(c). The results demonstrated that the sensing electrode exhibited high sensitivities of 4.372 and 2.615 mA mM^{-1} cm^{-2} within linear ranges of 0.01–1 mM and 1–2.5 mM, respectively, along with a low detection limit of 1.49 μM, as shown in Fig. S6 (3SD/N, where SD is the standard deviation and N is the sensitivity).

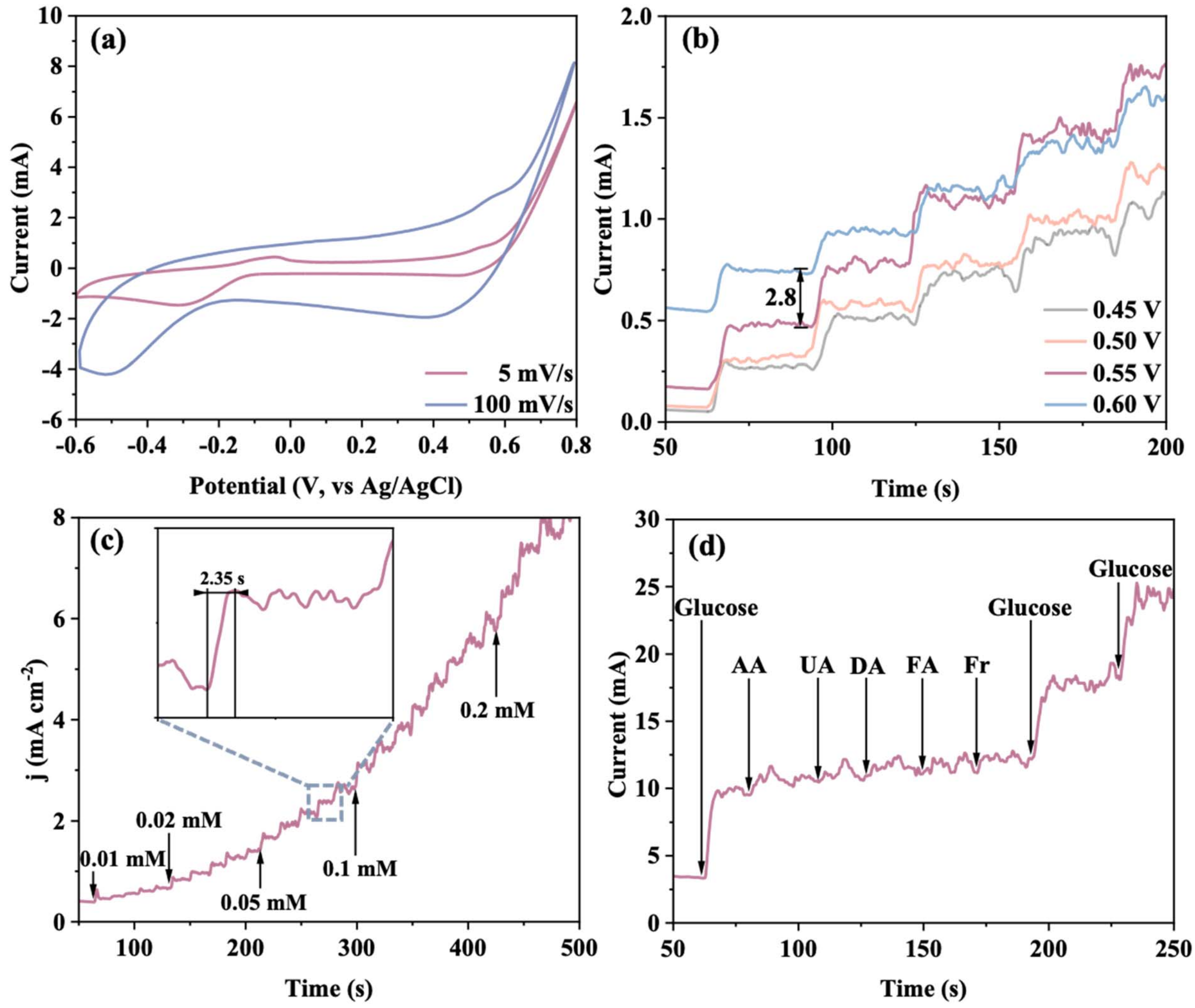

Fig. 3 Electrochemical performance of the sensor: (a) CV test, (b) *i*–*t* responses at different applied potentials, (c) *i*–*t* response curves toward glucose, and (d) anti-interference behavior in the presence of common interfering species.

Open Access Article. Published on 09 March 2026. Downloaded on 4/7/2026 1:56:55 PM.
This article is licensed under a Creative Commons Attribution-NonCommercial 3.0 Unported Licence.

Based on the electrochemical characterization and structural analysis, a plausible mechanism for glucose oxidation on Co_3O_{4-10}@PdO_5@CoCu oxides$_{\text{-}400}$ was proposed, as depicted in the following equation. Due to the P-type semiconductor properties of CuO, the increase in anode potential promoted the distortion of electron clouds on oxygen atoms, which led to the adsorption of OH^-. Electrons were transferred from CuO–OH^- to CuO, and the OH^- then oxidized glucose to gluconolactone.[29] Simultaneously, Co_3O_4 underwent electrochemical oxidation to form CoOOH, which was further oxidized to CoO_2. CoO_2, serving as an electron transfer mediator, was reduced to lower valence states while facilitating the oxidation of glucose to gluconolactone.[31,32] The incorporation of PdO significantly enhances the interfacial electron transfer kinetics between CuO and Co_3O_4 through synergistic trimetallic interactions, thereby improving the electrocatalytic performance for glucose oxidation, as shown in Fig. 4.[33–35]

$$\mathrm{CuO + OH^- \rightarrow (CuO{-}OH^-) + e^-} \tag{1}$$

$$\mathrm{CoO + OH^- \rightarrow CoOOH + H_2O + e^-} \tag{2}$$

$$\mathrm{CoOOH + OH^- \rightarrow CoO_2 + H_2O + e^-} \tag{3}$$

$$\mathrm{(CuO{-}OH^-) + glucose \rightarrow CuO + glucolactone} \tag{4}$$

$$\mathrm{CoO_2 + glucose \rightarrow CoOOH + glucolactone} \tag{5}$$

It is noteworthy that at elevated glucose concentrations, the accumulation of reaction intermediates may occur, potentially impeding the diffusion of oxidation products. This phenomenon accounts for the observed variations in glucose sensitivity across different concentration ranges, highlighting the concentration-dependent nature of the electrocatalytic process.

The practical application of non-enzymatic glucose sensors is critically dependent on their ability to maintain detection accuracy in the presence of various interfering substances commonly found in physiological samples. Therefore, the interference resistance of the Co_3O_{4-10}@PdO_5@CoCu oxides$_{\text{-}400}$ was assessed by the *i–t* test, depicted in Fig. 3(d). The experimental conditions were designed to simulate physiological environments of sweat, where the glucose concentration is typically an order of magnitude higher than that of potential interfering species. Accordingly, the measurements were performed by sequentially introducing 1 mM glucose and 0.1 mM concentrations of common interfering substances (UA, AA, FA, Fr, and DA) under continuous stirring conditions. The results demonstrated an immediate distinct response current upon each addition of glucose. In contrast, when the interfering substances were gradually added, negligible response current was observed from the sensing electrode. These tests confirmed that the presence of these interfering substances did not affect glucose detection and showcased excellent selectivity of the prepared sensing structure.

To investigate the effect of doping concentrations of PdO (0, 2.5, 5, 10 mM) on sensing sensitivity, *i–t* tests were conducted, as shown in Fig. 5(a). The sensitivities of PdO_x@CoCu oxides$_{\text{-}400}$ ($x =$ 0, 2.5, 5, 10) for glucose within the linear range of 0.01–1 mM were 2.756, 3.063, 4.238, and 2.618 mA mM^{-1} cm^{-2}, respectively. Among these samples, the highest sensitivity was achieved at a doping concentration of 5 mM. This enhancement is attributed to the balance between structural evolution and kinetic optimization. The incorporation of PdO induces a nanoscale Kirkendall effect, which generates structural defects and increases porosity. At the optimal concentration of 5 mM, these defects significantly enhance the mass transfer kinetics of glucose molecules and maximize the exposure of active sites while preserving the essential conductive skeleton of the MOF derivative. However, theoretical and morphological analyses suggest a threshold effect, indicating that when the doping concentration increases to 10 mM, the excessive etching leads to the collapse of the supporting framework (Fig. S3). This structural degradation impedes electron transfer pathways and reduces the effective surface area available for the redox reaction, thereby diminishing the sensing performance. Thus, 5 mM represents the optimal kinetic equilibrium point. Building upon these optimizations, the effect of electrodes with different doping concentrations of PdO and the sandwich MOF structure on sensing was further evaluated.

The sensitivities of the sandwich-structured Co_3O_{4-10}@PdO_x@CoCu oxides$_{\text{-}400}$ ($x = 0$, 2.5, 5, 10) to glucose within the

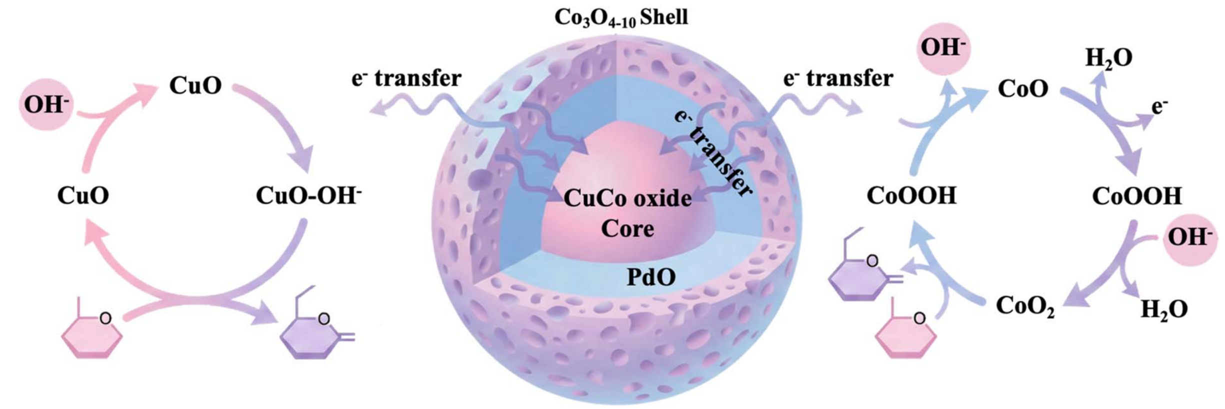

Fig. 4 The sensing mechanism of Co_3O_{4-10}@PdO_5@CoCu oxides$_{\text{-}400}$.

© 2026 The Author(s). Published by the Royal Society of Chemistry

Open Access Article. Published on 09 March 2026. Downloaded on 4/7/2026 1:56:55 PM.
This article is licensed under a Creative Commons Attribution-NonCommercial 3.0 Unported Licence.

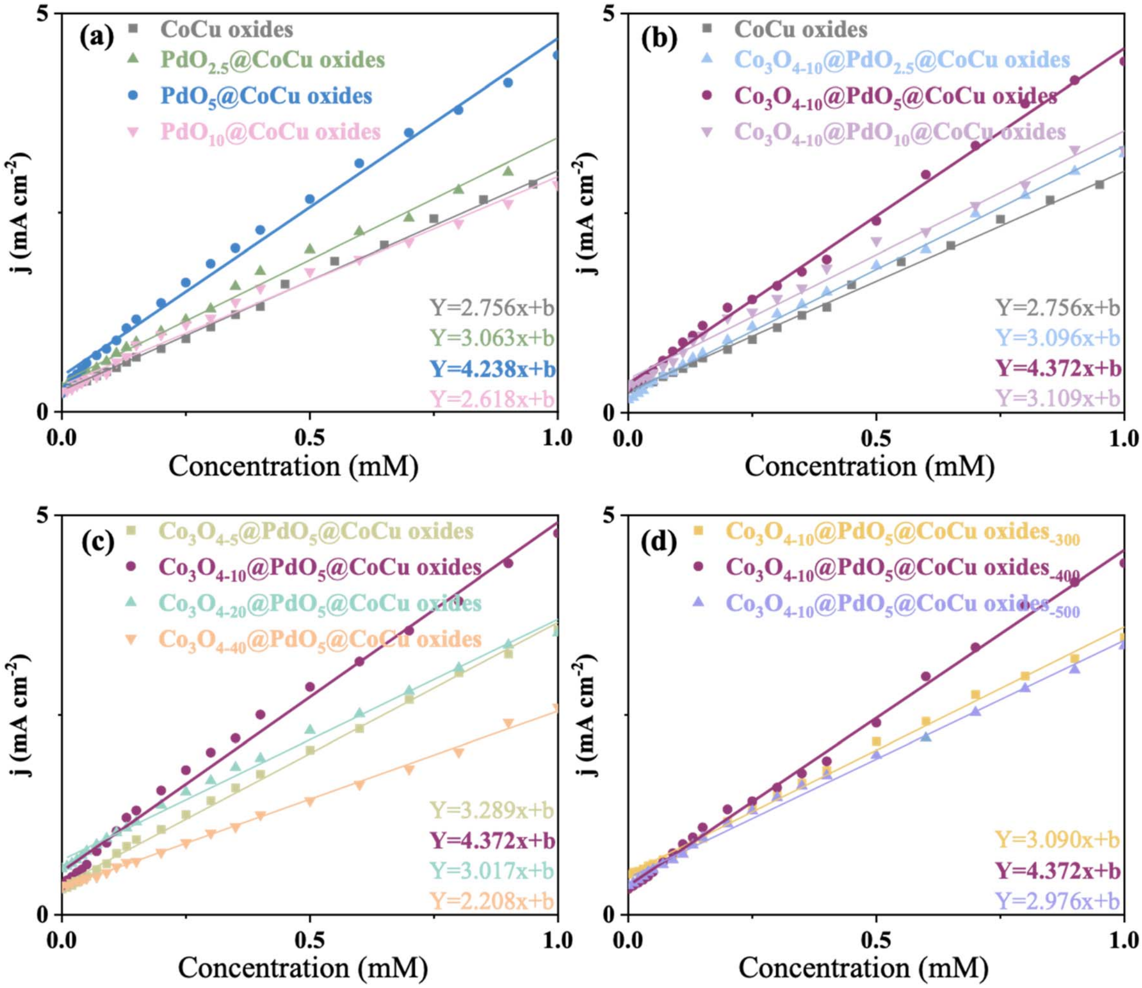

Fig. 5 The calibration curves of current *vs.* glucose concentration for (a) PdO$_x$@CoCu oxides$_{\text{-400}}$ ($x = 0, 2.5, 5, 10$), (b) Co$_3$O$_{4-10}$@PdO$_x$@CoCu oxides$_{\text{-400}}$ ($x = 0, 2.5, 5, 10$), (c) Co$_3$O$_{4-y}$@PdO$_5$@CoCu oxides$_{\text{-400}}$ ($y = 5, 10, 20, 40$), and (d) Co$_3$O$_{4-10}$@PdO$_5$@CoCu oxides$_{\text{-}z}$ ($z = 300, 400, 500$).

linear range of 0.01–1 mM were 2.756, 3.096, 4.372, and 3.109 mA mM^{-1} cm^{-2}, respectively, as shown in Fig. 5(b). The results verified that the sandwich structure exhibited higher sensitivities compared to direct doping of PdO, with the trends consistent with the direct doping results. The enhanced performance can be attributed to the strategic use of ZIF-L as a shell layer, which effectively immobilized PdO and prevented nanoparticle aggregation. This configuration not only increased the accessibility of active sites but also optimized mass transfer efficiency, as structurally confirmed by XRD (Fig. S2). Consequently, Co$_3$O$_{4-10}$@PdO$_5$@CoCu oxides$_{\text{-400}}$ exhibited the highest sensing sensitivity compared to other samples.

Additionally, the impact of different preparation times of the sandwich outer layer (5, 10, 20, 40 min) on the sensing performance of Co$_3$O$_{4-y}$@PdO$_5$@CoCu oxides$_{\text{-400}}$ ($y = 5, 10, 20, 40$) was investigated, as illustrated in Fig. 5(c). The results showed that the sensing sensitivity increased over time and reached its peak when the electrode was prepared for 10 min. However, further extension of the preparation time to 20 and 40 min resulted in a gradual decrease in sensitivity. This phenomenon can be attributed to the progressive thickening of the sandwich outer layer, which potentially impedes the electrochemical activity of PdO by limiting its accessibility during redox cycling. The 10 min preparation condition was identified as the optimal duration, as it achieved an ideal balance between PdO immobilization and accessibility. At this specific preparation time, the sensing structure effectively anchored PdO while maintaining sufficient exposure for electrochemical interactions, thereby establishing an efficient and stable ion transport pathway. This optimized configuration enabled the Co$_3$O$_{4-10}$@PdO$_5$@CoCu oxides$_{\text{-400}}$ to demonstrate exceptional electrochemical sensitivity, surpassing the performance of other preparation time variants.

Finally, the sensitivities of Co$_3$O$_{4-10}$@PdO$_5$@CoCu oxides$_{\text{-}z}$ ($z = 300, 400, 500$) with different annealing temperature were tested and found to be 3.090, 4.372, and 2.976 mA mM^{-1} cm^{-2} respectively, exhibited in Fig. 5(d). The enhanced sensitivity observed at 400 °C can be attributed to the complete decomposition of surface organic ligands, as indicated by the TGA curve (Fig. 2(b)), which simultaneously increased the

Open Access Article. Published on 09 March 2026. Downloaded on 4/7/2026 1:56:55 PM.
This article is licensed under a Creative Commons Attribution-NonCommercial 3.0 Unported Licence.

accessibility of active sites and improved ion transport efficiency. In contrast, at a lower temperature of 300 °C, the incomplete decomposition of organic linkers likely blocked the active sites. However, when further increasing temperature to 500 °C, the drastic weight loss in TGA suggests a collapse of the MOF-derived skeleton and agglomeration of metal oxides, resulting in a decrease in sensitivity. Thus, the electrochemical performance trend correlates well with the structural evolution predicted by thermal analysis. Therefore, the sample with a PdO doping concentration of 5 mM, an outer layer preparation time of 10 min, and an annealing temperature of 400 °C exhibited the optimum sensing performance.

Stability is a critical metric for evaluating the performance of a sensor, particularly under daily environmental conditions. To evaluate the effect of sandwich outer layer on the doping stability of the electrodes, i-t tests were conducted on $\mathrm{Co_3O_{4-y}}$-@$\mathrm{PdO_5}$@CoCu oxides$_{\text{-}400}$ ($y = 0, 5, 10, 20$) every three days over a period of 30 days, as illustrated in Fig. 6(a). The results of four different electrodes exhibited a decreasing trend in current response over time. Notably, the introduction of sandwich structures significantly mitigated this trend compared to $\mathrm{PdO_5}$@CoCu oxides$_{\text{-}400}$. The current attenuation trend decreased with the increase in the outer thickness of the sandwich structure, while $\mathrm{Co_3O_{4-10}}$@$\mathrm{PdO_5}$@CoCu oxides$_{\text{-}400}$ exhibited the least attenuation, maintaining 93.73% of the initial current response. This improvement may be attributed to the well-defined pore structure of MOFs, which contributes to maintaining catalytic stability. On the other hand, the sandwich structure provides substantial protection for PdO, which effectively prevents its migration and loss during the electrochemical reaction process. By controlling the thickness of the outer ZIF layer on PdO nanoparticles, it was proposed that the physical barrier provided by the sandwich structure and the interaction between PdO and ZIF could effectively prevent the aggregation and leaching of nanoparticles during the reaction.[36] It has been demonstrated that the sandwich heterogeneous structure is beneficial for enhancing electrochemical stability. To further examine the redox reaction mechanisms and structural stability, continuous CV tests were also performed on electrodes with and without sandwich heterostructures within the range of −0.6–0.8 V. As shown in Fig. 6(b) and S7, the evolution of redox peaks reveals distinct electrochemical behaviors. For the pristine $\mathrm{PdO_5}$@CoCu oxides$_{\text{-}400}$, the redox peak currents exhibited a sharp decline accompanied by a collapse in peak shape, suggesting the irreversible loss of active sites caused by the aggregation or leaching of PdO during the repeated redox cycles. In strong contrast, the sandwich-structured $\mathrm{Co_3O_{4-10}}$-@$\mathrm{PdO_5}$@CoCu oxides$_{\text{-}400}$ maintained well-defined redox peaks with minimal current decay. After 10 000 cycles, the anodic peak current of $\mathrm{PdO_5}$@CoCu oxides$_{\text{-}400}$ decreased significantly by 38.697%, whereas the sandwich structure only experienced an 11.415% reduction. The preservation of sharp redox peaks indicates that the sandwich architecture suppresses irreversible oxide phase transformations.[37] This comparative analysis confirms that the outer MOF-derived shell effectively confines the PdO, preserving the integrity of the redox active sites and ensuring long-term electrochemical stability.

To evaluate the reproducibility of the obtained sample, three electrodes were prepared as parallel electrodes under the same conditions, as shown in Fig. S8. The relative standard deviation (RSD) was calculated as 6.61% after introducing the same concentration of glucose, which proved that $\mathrm{Co_3O_{4-10}}$@$\mathrm{PdO_5}$@-CoCu oxides$_{\text{-}400}$ have excellent repeatability. Compared with other similar electrodes, the structure prepared in this work was found to have remarkable advantages in terms of the stability, sensitivity, and response time, as shown in Table 1.

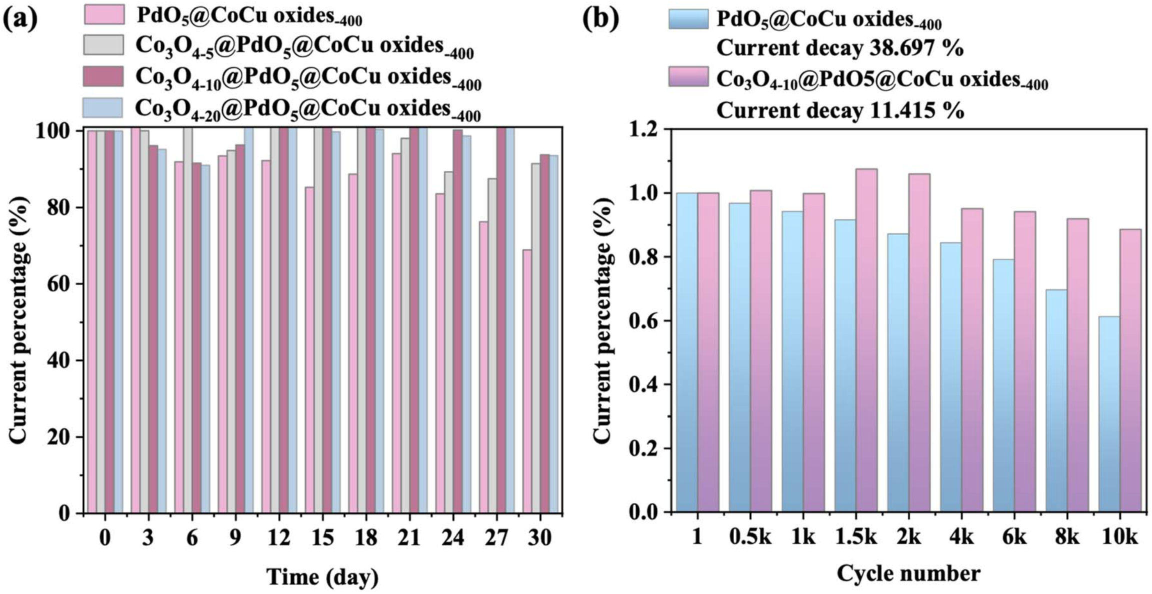

Fig. 6 (a) Long-term stability of $\mathrm{Co_3O_{4-y}}$@ $\mathrm{PdO_5}$@CoCu oxides$_{\text{-}400}$, and (b) changes in anodic peak current for $\mathrm{PdO_5}$@CoCu oxides$_{\text{-}400}$ and $\mathrm{Co_3O_{4-10}}$@$\mathrm{PdO_5}$@CoCu oxides$_{\text{-}400}$.

© 2026 The Author(s). Published by the Royal Society of Chemistry

Open Access Article. Published on 09 March 2026. Downloaded on 4/7/2026 1:56:55 PM.
This article is licensed under a Creative Commons Attribution-NonCommercial 3.0 Unported Licence.

Table 1 Various electrochemical detection platforms for glucose sensing

Electrode structure	Sensitivity (μA mM^{-1} cm^{-2})	Stability	Response time (s)	LOD (μM)	Linear range (mM)	Ref.
Co-MOF	169	90% after 7 days	7	1.6	0.005–0.9	38
Co-MOFs	160.75	77.33% after 15 days	3	3.2	0.010–1.2	39
Cu@Co-MOF	282.89	69.25% after 15 days	7	1.6	0.005–0.4	40
Ni/Co-FAMOF	366	93.8% after 27 days		2	0.006–1.004	41
Au@Ni-BTC	1447.1			1.5	0.005–7.4	42
AgNPs@NiCo-MOF	1191.84	77.63% after 28 days	4	2.3	0.005–1.125	43
GOx-rGO/Pt NPs@Zn-MOF-74	64.51		40	1.8	0.006–6	44
N–Co-MOF@PDA-Ag	183.6	96.2% after 3600 s		0.5	0.001–2	45
Pd-CoCNTs	75.4	88.8% after 96 h	5	1	0.010–2.4	46
PtRhNi/GNS	110.5	83.6% after 30 days		18.9	0.06–0.15	47
$Co_3O_{4\text{-}10}$@PdO_5@CoCu oxides$_{\text{-}400}$	4398	93.73% after 30 days	2.35	1.49	0.01–1	This work

Conclusions

In this study, we proposed a novel preparation method for MOF-based sandwich heterostructures. The composite structure of $Co_3O_{4\text{-}10}$@PdO_5@CoCu oxides$_{\text{-}400}$ was characterized by various techniques and successfully applied to electrochemical glucose detection. A systematic investigation was conducted to evaluate the influence of key parameters, including the doping concentration of PdO, thickness of the ZIF-L outer layer, and annealing temperature, on the doping stability and sensing performance of the electrode. We found that the incorporated PdO significantly enhanced the sensitivity, which can be attributed to the synergistic effects among the trimetallic oxides. Moreover, the well-defined pore structure of the sandwich MOF prevented PdO aggregation during sintering, which improved the efficiency of electron transfer. Additionally, more active sites were exposed by annealing-induced structural transformations, which further enhanced the performance of electrochemical sensing. The prepared electrode exhibited high sensitivity of 4.372 mA mM^{-1} cm^{-2} and 2.615 mA mM^{-1} cm^{-2} within linear ranges of 0.01–1 mM and 1–2.5 mM, respectively, along with a rapid response time of 2.35 s. The effect of shell thickness on the doping stability of the electrode was further investigated. Remarkably, the electrode maintained 93.73% of its initial current response after 30 days, demonstrating excellent long-term stability due to the suppressed PdO leaching during electrochemical reactions. This exceptional durability, combined with the flexible substrate, positions the heterostructure as a viable candidate for wearable sensors. Despite these promising results, the current study is limited to laboratory settings. To bridge the gap toward practical deployment, our future work will first prioritize rigorously validating the sensor's accuracy and anti-biofouling properties in human sweat to address potential matrix effects. In parallel, we plan to integrate the flexible electrode with microfluidic sampling interfaces and wireless signal transmission modules to construct a fully autonomous wearable system. Ultimately, our work overcomes the critical stability bottleneck at the material level, offering a promising pathway toward reliable, non-invasive continuous glucose monitoring.

Author contributions

Jiaxi Li: visualization, writing – original draft, formal analysis, investigation. Chen Chen: funding acquisition, writing – review and editing, conceptualization. Zirong Tang: project administration, resources. Guanglan Liao: project administration, resources, writing – review and editing. Tielin Shi: project administration. Lei Nie: project administration, resources, supervision.

Conflicts of interest

The authors declare that there is no conflict of interest.

Data availability

Data available on request from the authors.

Supplementary information (SI) is available. See DOI: https://doi.org/10.1039/d5ra10005d.

Acknowledgements

This study was supported by the Open Fund of Hubei Modern Manufacturing Quality Laboratory (No. KFJJ-2022016), and the Doctoral Start-up Fund of Hubei Modern Manufacturing Quality Laboratory (No. XJ2021005501).

References

1 E. Sehit and Z. Altintas, Significance of Nanomaterials in Electrochemical Glucose Sensors: An Updated Review (2016-2020), *Biosens. Bioelectron.*, 2020, **159**, 112165.

2 H. Sun, P. Saeedi, S. Karuranga, M. Pinkepank, K. Ogurtsova, B. B. Duncan, C. Stein, A. Basit, J. C. N. Chan, J. C. Mbanya, M. E. Pavkov, A. Ramachandaran, S. H. Wild, S. James, W. H. Herman, P. Zhang, C. Bommer, S. Kuo, E. J. Boyko and D. J. Magliano, IDF Diabetes Atlas: Global, Regional and Country-level Diabetes Prevalence Estimates for 2021 and Projections for 2045, *Diabetes Res. Clin. Pract.*, 2022, **183**, 109119.

© 2026 The Author(s). Published by the Royal Society of Chemistry

Open Access Article. Published on 09 March 2026. Downloaded on 4/7/2026 1:56:55 PM.
This article is licensed under a Creative Commons Attribution-NonCommercial 3.0 Unported Licence.

3 J. He, X. Xu, M. Li, S. Zhou and W. Zhou, Recent Advances in Perovskite Oxides for Non-enzymatic Electrochemical Sensors: A Review, *Anal. Chim. Acta*, 2023, **1251**, 341007.

4 Y. Zhao, Y. Jiang, Y. Mo, Y. Zhai, J. Liu, A. C. Strzelecki, X. Guo and C. Shan, Boosting Electrochemical Catalysis and Nonenzymatic Sensing Toward Glucose by Single-Atom Pt Supported on Cu@CuO Core-Shell Nanowires, *Small*, 2023, **19**, 2207240.

5 Z. Li, W. Zeng and Y. Li, Recent Progress in MOF-Based Electrochemical Sensors for Non-Enzymatic Glucose Detection, *Molecules*, 2023, **28**, 4891.

6 D. Wang, Y. Wang, W. Dube, J. Zhang, J. Gao, X. Tang, G. Urujeni, Y. Zhang, L. Zhao, H. He, D. Xiao and P. A. Dramou, Smart Nanocomposite System for Controlled Insulin Release and Glucose Sensing in Diabetes Management, *Nanoscale*, 2025, **17**, 16213–16222.

7 P. G. Le and S. Cho, Recent Developments in MXene-Based Enzyme-Free Electrochemical Glucose Sensing, *BioChip J.*, 2024, **18**, 521–534.

8 N. M. Kilic, S. Singh, G. Keles, S. Cinti, S. Kurbanoglu and D. Odaci, Novel Approaches to Enzyme-Based Electrochemical Nanobiosensors, *Biosensors*, 2023, **13**, 622.

9 C. Jeganathan, H. Mitsuboshi, H. Yamamoto, Y. Motoyama, K. Kokado, M. Hara and M. Yoshimura, Hydrogen-Substituted Graphdiyne Encapsulated Cu_2O Nanowires as Binder-Free Electrodes for Non-Enzymatic Glucose Sensing, *ACS Appl. Nano Mater.*, 2024, **7**, 20665–20677.

10 X. Xu, C. Zhang, W. Yang, Y. Li, Y. Haldorai, J. Zhenyu and W. Xie, Nanofiber-shaped Co_3O_4@In_2O_3 Composite for High-performance Enzymeless Glucose Sensing, *Nanoscale*, 2025, **17**, 6718–6726.

11 H. Huu Do, S. Y. Kim and Q. V. Le, Development of Non-precious Metal Oxide-based Electrodes for Enzyme-free Glucose Detection: A Review, *Microchem. J.*, 2023, **193**, 109202.

12 M. Govindaraj, A. Srivastava, M. K. Muthukumaran, P. Tsai, Y. Lin, B. K. Raja, J. Rajendran, V. K. Ponnusamy and J. Arockia Selvi, Current Advancements and Prospects of Enzymatic and Non-enzymatic Electrochemical Glucose Sensors, *Int. J. Biol. Macromol.*, 2023, **253**, 126680.

13 S. Balachandran, K. Jothi, S. Muthamizh, A. Subhasri, R. Kumar, A. Kumar, M. Wadaan and C. Hu, Facile fabrication of $BiVO_4$ Microspheres: Investigating their twin application on potential in electrochemical capacitors and protein detection, *J. Power Sources*, 2025, **650**(15), 237481.

14 Shubhangi, I. Nandi, S. K. Rai and P. Chandra, MOF-based Nanocomposites as Transduction Matrices for Optical and Electrochemical Sensing, *Talanta*, 2024, **266**, 125124.

15 W. Dai, B. Wu, F. Zhang, Y. Huang, C. Zhao, Y. Zhang, C. Cui, J. Guo and S. Huang, Construction of Bimetallic Oxy-hydroxides Based on $Ni(OH)_2$ Nanosheets for Sensitive Non-Enzymatic Glucose Detection via Electrochemical Oxidation and Incorporation, *Nanoscale*, 2025, **17**, 2589–2598.

16 Y. Wang, T. Sun, A. Mostaghimi, T. Goncalves, Z. Liang, Y. Zhou, W. Zhang, Z. Huang, Y. Ma, R. Cao, S. Siahrostami and H. Zheng, Two-Dimensional Metal-Organic Frameworks with Unique Oriented Layers for Oxygen Reduction Reaction: Tailoring the Activity through Exposed Crystal Facets, *CCS Chem.*, 2022, **4**, 1633–1642.

17 C. Chen, J. Li, Z. Tang, G. Liao and L. Nie, In-situ Co-precipitation of Bi-MOF Derivatives for Highly Sensitive Electrochemical Glucose Sensing, *Microchem. J.*, 2024, **199**, 109897.

18 T. Rasheed and K. Rizwan, Metal-organic Frameworks Based Hybrid Nanocomposites as State-of-the-art Analytical Tools for Electrochemical Sensing Applications, *Biosens. Bioelectron.*, 2022, **199**, 113867.

19 C. Chen, Y. Zhong, S. Cheng, Y. Huang, T. Li, T. Shi, G. Liao and Z. Tang, In Situ Fabrication of Porous Nanostructures Derived from Bimetal-Organic Frameworks for Highly Sensitive Non-Enzymatic Glucose Sensors, *J. Electrochem. Soc.*, 2020, **167**, 027531.

20 Y. Xu, Q. Li and H. Pang, Recent Advances in Metal Organic Frameworks and Their Composites for Batteries, *Nano Futures*, 2020, **4**, 32007.

21 M. Mohideen, C. Santhosh, A. Radhamani, C. Wang, P. Hu, B. Subramanian, S. Ramakrishna and Y. Liu, Negative Impact of Sulfur Doping on ORR/OER Performance in Dual-active-site Co-MOF/MXene Electrocatalysts, *J. Colloid Interface Sci.*, 2026, **703**, 139165.

22 F. Wang, X. Ding, X. Niu, X. Liu, W. Wang and J. Zhang, Green Preparation of Core-shell Cu@Pd Nanoparticles with Chitosan for Glucose Detection, *Carbohydr. Polym.*, 2020, **247**, 116647.

23 Z. Li, X. Zhao, X. Jiang, Y. Wu, C. Chen, Z. Zhu, J. Marty and Q. Chen, An Enhanced Nonenzymatic Electrochemical Glucose Sensor Based on Copper-Palladium Nanoparticles Modified Glassy Carbon Electrodes, *Electroanalysis*, 2018, **30**, 1811–1819.

24 C. Nandhini, P. Arul, S. Huang, M. Tominaga and C. Huang, Electrochemical Sensing of Dual Biomolecules in Live Cells and Whole Blood Samples: a Flexible Gold Wire-Modified Copper-organic Framework-based Hybrid Composite, *Bioelectrochemistry*, 2023, **152**, 108434.

25 X. Chen, X. Feng, T. Zhan, Y. Xue, H. Li, G. Han, Z. Chen and H. Kraatz, Construction of a Portable Enzyme-free Electrochemical Glucose Detection System Based on the Synergistic Interaction of Cu-MOF and PtNPs, *Sens. Actuators, B*, 2023, **395**, 134498.

26 Y. Wang, H. Li, Z. Hu, X. Chen, Z. Sun, Y. Ai, W. Xu, W. Zhang, K. Ding, C. Li, T. Jiang, S. Zhao, H. Wang, G. Zhang and H. Sun, Selective Transfer Hydrogenation of Nitro benzaldehydes Over an Extremely Active Synergistic MOF@Pt@MOF Catalyst, *Microporous Mesoporous Mater.*, 2022, **346**, 112322.

27 Z. Zhang, J. Dou and H. Zhang, Mixed Membranes Comprising Carboxymethyl Cellulose (as Capping Agent and Gas Barrier Matrix) and Nanoporous ZIF-L Nanosheets for Gas Separation Applications, *Polymers*, 2018, **10**, 1340.

28 C. Wijaya, S. Ismadji, H. Aparamarta and S. Gunawan, Facile and Green Synthesis of Starfruit-Like ZIF-L, and Its Optimization Study, *Molecules*, 2021, **26**, 4416.

© 2026 The Author(s). Published by the Royal Society of Chemistry

Open Access Article. Published on 09 March 2026. Downloaded on 4/7/2026 1:56:55 PM.
This article is licensed under a Creative Commons Attribution-NonCommercial 3.0 Unported Licence.

29 Y. Wen, W. Cheng, Y. Wang, F. Shen and Y. Lan, Tailoring the Hydrophobic Interface of Core-shell HKUST-1@Cu_2O Nanocomposites for Efficiently Selective CO_2 Electroreduction, *Small*, 2024, **20**, 2307467.

30 B. Chen, X. Zeng, Y. Liu, F. Xiao, M. Huang, K. Bing Tan, D. Cai, J. Huang and G. Zhan, Thermal Decomposition Kinetics of M-BTC (M = Cu, Co, Zn, and Ce) and M-BTC/Pt Composites Under Oxidative and Reductive Environments, *Chem. Eng. J.*, 2022, **450**, 138470.

31 G. Anbalagan, Z. Xu, J. Kumaravel, V. Suresh, B. Subramanian, N. Sandhiran, S. Devanesan, M. AlSalhi and M. Yang, Hydrothermal synthesis of $InVO_4/Bi_2S_3$ heterojunctions for enhanced efficiency in visible-light photocatalysis and hydrogen evolution reactions, *J. Power Sources*, 2025, **647**(15), 237346.

32 S. Balachandran, K. Jothi, M. Albeshr, G. Anbalagan, R. Kumar, N. Prakash and A. Kumar, Evaluation of nitrogen-doped cobalt oxide with a flower-like architecture for high-performance supercapacitors, *J. Energy Storage*, 2025, **120**(1), 116479.

33 M. Mohideen, A. Qadir, B. Subramanian, S. Ramakrishna and Y. Liu, Nitrogen and sulfur incorporated chitosan-derived carbon sphere hybrid MXene as highly efficient electrocatalyst for oxygen reduction reaction, *Mater. Today Phys.*, 2024, **46**, 101528.

34 D. Wang, H. Zhao, L. Guo, L. Zhang, H. Zhao, X. Fang, S. Li and G. Wang, Facile Synthesis of CuO-Co_3O_4 Prickly-Sphere-like Composite for Non-enzymatic Glucose Sensors, *Rare Met.*, 2022, **41**, 1911–1920.

35 J. T. C. Jr Barragan, S. Kogikoski, E. T. S. G. Da Silva and L. T. Kubota, Insight into the Electro-oxidation Mechanism of Glucose and Other Carbohydrates by CuO-Based Electrodes, *Anal. Chem.*, 2018, **90**, 3357–3365.

36 Y. Yun, H. Sheng, K. Bao, L. Xu, Y. Zhang, D. Astruc and M. Zhu, Design and Remarkable Efficiency of the Robust Sandwich Cluster Composite Nanocatalysts ZIF-8@Au25@ZIF-67, *J. Am. Chem. Soc.*, 2020, **142**, 4126–4130.

37 F. Sun, X. Wang, Z. You, H. Xia, S. Wang, C. Jia, Y. Zhou and J. Zhang, Sandwich Structure Confined Gold as Highly Sensitive and Stable Electrochemical Non-Enzymatic Glucose Sensor with Low Oxidation Potential, *J. Mater. Sci. Technol.*, 2022, **123**, 113–120.

38 L. Zhang, N. Wang, P. Cao, M. Lin, L. Xu and H. Ma, Electrochemical Non-enzymatic Glucose Sensor Using Ionic Liquid Incorporated Cobalt-based Metal-organic Framework, *Microchem. J.*, 2020, **159**, 105343.

39 Z. Ma, Y. Ma, B. Liu, L. Xu and H. Jiao, A High-performance Co-MOF Non-enzymatic Electrochemical Sensor for Glucose Detection, *New J. Chem.*, 2021, **45**, 21350–21358.

40 Z. Ma, Y. Wang, B. Liu, H. Jiao and L. A. Xu, Non-Enzymatic Electrochemical Sensor of Cu@Co-MOF Composite for Glucose Detection with High Sensitivity and Selectivity, *Chemosensors*, 2022, **10**, 416.

41 S. Song, X. Ma, W. Li, B. Zhang, B. Shao, X. Chang and X. Liu, Novel Stylophora Coral-like Furan-based Ni/Co Bimetallic Metal Organic Framework for High-performance Capacitive Storage and Non-enzymatic Glucose Electrochemical Sensing, *J. Alloy. Compd.*, 2023, **931**, 167413.

42 J. Chen, H. Yin, J. Zhou, L. Wang, J. Gong, Z. Ji and Q. Nie, Efficient Nonenzymatic Sensors Based on Ni-MOF Microspheres Decorated with Au Nanoparticles for Glucose Detection, *J. Electron. Mater.*, 2020, **49**, 4754–4763.

43 Y. Ma, Y. Leng, D. Huo, D. Zhao, J. Zheng, P. Zhao, H. Yang, F. Li and C. Hou, A Portable Sensor for Glucose Detection in Huangshui Based on Blossom-shaped Bimetallic Organic Framework Loaded with Silver Nanoparticles Combined with Machine Learning, *Food Chem.*, 2023, **429**, 136850.

44 D. Uzak, A. Atiroğlu, V. Atiroğlu, B. Çakıroğlu and M. Özacar, Reduced Graphene Oxide/Pt Nanoparticles/Zn-MOF-74 Nanomaterial for a Glucose Biosensor Construction, *Electroanalysis*, 2020, **32**, 510–519.

45 X. Zhai, Y. Cao, W. Sun, S. Cao, Y. Wang, L. He, N. Yao and D. Zhao, Core-shell Composite N-doped-Co-MOF@polydopamine Decorated with Ag Nanoparticles for Nonenzymatic Glucose Sensors, *J. Electroanal. Chem.*, 2022, **918**, 116491.

46 B. Huang, Y. Wang, Z. Lu, H. Du and J. Ye, One Pot Synthesis of Palladium-cobalt Nanoparticles Over Carbon Nanotubes as a Sensitive Non-enzymatic Sensor for Glucose and Hydrogen Peroxide Detection, *Sens. Actuators, B*, 2017, **252**, 1016–1025.

47 K. Lu, Z. Liu and Y. Shen, Bifunctional Platinum-based Catalysts for Electrochemical Detection and Conversion of Glucose, *Microchem. J.*, 2025, **212**, 113389.

© 2026 The Author(s). Published by the Royal Society of Chemistry